

***Final Draft***  
**of the original manuscript:**

Wang, L.; Zenk, C.; Stark, A.; Felfer, P.; Gabrisch, H.; Goeken, M.;  
Lorenz, U.; Pyczak, F.:

**Morphology evolution of Ti<sub>3</sub>AlC carbide precipitates in high  
Nb containing TiAl alloys**

In: Acta Materialia (2017) Elsevier

DOI: 10.1016/j.actamat.2017.07.018

# Morphology evolution of Ti<sub>3</sub>AlC carbide precipitates in high Nb containing TiAl alloys

\*Li Wang<sup>1</sup>, Carolin Zenk<sup>2</sup>, Andreas Stark<sup>1</sup>, Peter Felfer<sup>2</sup>, Heike Gabrisch<sup>1</sup>, Mathias Göken<sup>2</sup>, Uwe Lorenz<sup>1</sup>, Florian Pyczak<sup>1,3</sup>

<sup>1</sup>Institute of Materials Research, Helmholtz-Zentrum Geesthacht, Max-Planck-Strasse 1, Geesthacht, D-21502, Germany

<sup>2</sup>Friedrich-Alexander-Universität Erlangen-Nürnberg (FAU), Materials Science and Engineering, Institute I, Germany

<sup>3</sup>Brandenburgisch Technische Universität Cottbus-Senftenberg, Konrad-Wachsmann-Allee 17, Cottbus, D-03046, Germany

\* Corresponding author: Tel.: +49 04152-87-2672; fax: +49 04152-87-2534

E-Mail: Li.wang1@hzg.de (Li Wang)

## Abstract

This work elucidates the morphology evolution of perovskite Ti<sub>3</sub>AlC carbides in a Ti-45Al-5Nb-0.75C alloy during ageing at 800 °C. The carbides in the  $\gamma$  matrix are initially needle-shaped with their long axis parallel to the [001] lattice direction of the  $\gamma$  matrix. After extended annealing, they decompose into small carbide sub-particles. By combining different transmission electron microscopy characterization methods and atom probe tomography it has been verified that the carbides first split into several parallel needles that are aligned along the [001] <sub>$\gamma$</sub>  lattice direction. Later these parallel needles further decompose into numerous small sub-particles, while the matrix phase region between the sub-particles crystallographically reorients. To the authors'

knowledge this is the first work which demonstrates such a precipitate splitting process in a matrix with a tetragonal crystal structure. It is proposed that the decomposition into small sub-particles is energetically favorable owing to the elastic interaction energy between the split sub-particles.

### **Keywords**

Titanium aluminides; Carbides; Morphology; Splitting; Transmission electron microscopy

## **1. Introduction**

Recently  $\gamma$ -TiAl alloys have been applied successfully in commercial aircraft engines as low pressure turbine blades [1] and are considered as promising substitutes for Ni-base superalloys. To further raise their application temperature and improve their hot-workability and castability through  $\beta$  phase solidification [2],  $\gamma$ -TiAl alloys with a high amount of Nb (5-10 at. %) have been developed. These alloys possess high strength [3], excellent creep resistance [4] and good oxidation behavior [5] at elevated temperatures. Nevertheless, a further increase of the application temperature is still an attractive goal of  $\gamma$ -TiAl alloy development. The creep properties of  $\gamma$ -TiAl based alloys are improved by the addition of carbon via precipitation hardening by the  $\text{Ti}_3\text{AlC}$  perovskite (P-) phase [6, 7]. During deformation P-type carbides interact with dislocations, pin them and prevent dislocation propagation [4]. Appel et al. [8, 9] showed that the high density of needle-like perovskite precipitates in  $\gamma$ -TiAl alloys could also act as heterogeneous nucleation sites for mechanical nano-twins, which could release stress concentrations and thus support plastic deformation of  $\gamma$ -TiAl alloys. The P-type carbides initially precipitate coherently in the  $\gamma$  matrix and have a needle-like shape with a high aspect

ratio [7, 10, 11]. In the course of extended annealing they coarsen and finally lose coherency [10]. In TiAl alloys with 0.5 mol% C Tian et al. [11] detected a long-range ordering of carbon-vacancies in the P-Ti<sub>3</sub>AlC carbides and two ordered domains coexisting in a single needle after annealing at 800 °C. But this phenomenon disappeared at higher temperatures of around 900 °C [11]. The chemical composition of the domain boundaries and internal domains of a needle-like P-type carbide in TiAl has been studied using atom probe tomography by Gerstl et al. [12]. The authors found that after ageing at 800 °C for 24 h, the chemical composition within the domains differed from the domain boundaries. After annealing for 48 h, the composition fluctuation across the domain boundaries was greatly reduced. They believed that initial changes of chemical composition across the domain boundaries was an initial step in the phase transformation from perovskite (P-) type to hexagonal (H-) type carbides [12].

To date research on carbides in TiAl alloys has mainly concentrated on the ternary Ti-Al-C system [11], with only limited information about long-term carbide morphology development in some multinary systems [13-16]. Also information about the carbide morphology development on time scales in excess of one week is scarce. An understanding of carbide morphology development and the shape stability of perovskite Ti<sub>3</sub>AlC carbides is essential for further improving the mechanical properties of TiAl based alloys. According to stability considerations, needle-shaped precipitates with a high aspect ratio that are present in TiAl alloys could be prone to morphological instability after long-term annealing treatments. Such an instability would be particularly important with respect to the long-term creep resistance of the alloys. Thus in this work, we have investigated the evolution of the perovskite Ti<sub>3</sub>AlC carbide morphology in a Ti-45Al-5Nb-0.75C (all in atomic percent) alloy over the course of

long-term aging at 800 °C using transmission electron microscopy (TEM), high resolution TEM (HRTEM) and high-energy X-ray diffraction (HEXRD). The local chemical composition of the precipitates and their surrounding area was determined using atom probe tomography (APT).

## **2. Experimental**

The investigated alloy has a composition of Ti-45Al-5Nb-0.75C (in atomic percent) and was produced using the powder metallurgy (PM) route. Pre-alloyed powder was made by plasma melting induction guiding gas atomization (PIGA) and then consolidated using hot-isostatic pressing (HIP) at 1250 °C and 200 MPa for 2 h. The actual carbon content was measured to be 2170 µg/g (0.74 at. %) and the nitrogen concentration was 48 µg/g in the HIPed powder (0-180 µm) using the LECO CS-444 melt extraction system. More detailed information about the material production and the microstructure after HIPing can be found in [17-19]. In order to form finely dispersed precipitates in the  $\gamma$  matrix, different heat treatments were done with specimens cut from the HIPed billet. Specimens had a size of around 10\*10\*10 mm<sup>3</sup> and the microstructure investigated was close to the center to avoid side effects from possible nitrogen pick-up. Some specimens were directly annealed at 800 °C for 24, 48, 96, 168, 336 or 1054 h, followed by furnace cooling. Such specimens are denoted as HIP+anneal. To dissolve the primary carbides present in the HIPed state another series of specimens were first solution-treated at 1250 °C for 5 h, followed by oil quenching and subsequently aged at 800 °C for 24, 48, 96, 168, 336 or 1054 h. These specimens are denoted by SOL+anneal. All the heat treatments were performed in air.

High-energy X-ray diffraction experiments to determine lattice parameters were carried out at the HEMS and HARWI-II beam lines run by the Helmholtz-Zentrum Geesthacht at the Deutsches Elektronen-Synchrotron (DESY) in Hamburg. The X-ray beams had a cross section of  $1 \times 1 \text{ mm}^2$  and a photon energy of 87.1 keV at HEMS and 100 keV at HARWI-II. These energies correspond to X-ray wavelengths of 0.1425 Å and 0.1240 Å, respectively. The diffractograms were either recorded using a mar345 image plate or a PerkinElmer XRD 1622 flat panel detector at the HEMS beamline and a mar555 flat panel detector at HARWI-II. Rietveld analysis of the HEXRD patterns was used to determine the lattice parameters of the  $\gamma$  phase in the various specimens. Due to the low volume fraction of carbides, Rietveld analysis could not be used to determine the exact lattice parameters of the carbides. Thus, the lattice parameters of P-type carbides were determined as the average value from the peak positions of the (111), (200) and (220) reflections.

The number density, size and morphology of carbides were investigated using a Philips CM200 TEM operated at 200 kV. Carbide size and number density measurements were determined from TEM images and at least three  $\gamma$  grains were analyzed for each condition. The TEM images were recorded along the  $[100]_\gamma$  and  $[001]_\gamma$  lattice directions in order to measure the length (L) and diameter (D) of the carbide needles, and the length (L), width (W) and thickness (T) of the carbide plates. The number density of the precipitates was calculated from the number per unit area divided by the foil thickness when imaged along the  $[001]$  direction which could be approximated to be about 100 nm for all specimens. The values for each heat-treated condition were averaged from about 200-3000 carbides. More detailed information about the methods used to determine the carbide number density and size can be found

in [20]. The interface between the carbides and the  $\gamma$  matrix, and their atomic arrangement were examined in high resolution using a FEI Titan 80-300 TEM with a  $C_s$  image corrector operated at 300 kV. TEM specimens with 2.3 mm diameter were drilled out, mechanically ground to a thickness below 120  $\mu\text{m}$ , and then thinned by twin-jet electro-polishing at 25-35 V and a temperature of  $-40\text{ }^\circ\text{C}$  in a solution of 26 ml perchloric acid (70%), 359 ml 2-butanol and 625 ml methanol.

The atom probe analysis was carried out on a Cameca LEAP 4000X HR atom probe using high voltage pulses to trigger field evaporation. The experiments were done at a temperature of 65 K, with the voltage pulses set to 20% of the DC bias voltage. The voltage was regulated to register a detector hit on average in 0.9% of the pulses. The samples were prepared using standard FIB based lift-out methods with low-kV final steps to avoid ion damage in the investigated volume [21, 22].

### **3. Results and discussions**

#### **3.1 Development of $\text{Ti}_3\text{AlC}$ carbide size, density and morphology**

**Figure 1** shows the development of carbide morphology in  $\gamma$  grains in SOL+anneal specimens. After 24 hours annealing at  $800\text{ }^\circ\text{C}$ , needle-shaped carbides that are elongated along the c-axis of the  $\gamma$  matrix can be observed when imaged along the  $[100]_\gamma$  or  $[010]_\gamma$  direction. They have a diameter of about 4 nm and a length of about 20 nm (standard deviation  $< \pm 1.5$  nm). When imaged along the  $[001]_\gamma$  direction, the circular cross-section of these needles is visible. The carbides grow in size when annealing time is increased to 168 h. Viewing along the  $[001]_\gamma$  direction it can be seen that some carbide cross-sections are very close to each other and regularly spaced, seemingly as though a large carbide of plate-like morphology has split in parallel

needles. After 1054 hours of annealing large conglomerates consisting of numerous small carbide sub-particles are found instead of coarsened needles. They seem to have formed from the parallel needles found after 168 hours by splitting of these needles along their needle axis. The sub-particles are between 5 to 15 nm in diameter. For all ageing times, the P-type carbides exhibit the same orientation relationship with the  $\gamma$  matrix: namely  $[100]_{\gamma} // [100]_{\text{P}}$  and  $(001)_{\gamma} // (001)_{\text{P}}$ , as reported in literature [10, 11]. This was evidenced by analysis of diffraction patterns.

It is interesting to compare the morphology development with that in the HIP+anneal material. The different heat treatment history which probably leads to minor changes in carbon distribution significantly alters some details of the morphology development. The HIP+anneal material also contained needle-like shaped carbides after ageing at 800 °C for 24 h. But contrary to the solution-treated material a fully developed plate state of the carbides can be found prior to splitting into sub-particles (happening after 168 h), as shown in **Fig. 2**. There are two sets of carbide plates with the habit plane either parallel to the (100) or (010) crystallographic planes of the  $\gamma$  matrix (**Fig. 2a** and **Fig. 2b**). It has also been found that the morphology transformation of carbides from needles to plates first takes place close to grain boundaries, as shown in **Fig. 2c**. This is most probably due to the formation of large carbides at grain boundaries depleting regions near the grain boundaries in carbon. This variation in carbon content results in a lower density of carbides near grain boundaries. But these carbides grow faster, than those within the grain interior, and undergo morphological transformation to plates earlier. Such local differences in morphology development are not observed in the SOL+anneal specimens indicating that the local carbon concentration strongly

influences the carbide morphology development, presumably via influencing the Young's modulus and lattice parameters of the  $\gamma$  matrix and the P-type carbides.

The assumption of a needle-like shape along the  $[001]_{\gamma}$  direction during growth is well known from literature [11]. The lattice mismatch between the coherently embedded P-type carbide and the  $\gamma$  matrix is lower along this direction [11]. **Table 1** lists the lattice mismatch along the different crystallographic orientations between the P-type carbide and the  $\gamma$ -TiAl phase measured by HEXRD. The lattice mismatch along  $[100]$  and  $[001]$  directions is defined by:  $\varepsilon_{100}=(a_{\gamma}-a_P)/a_P$  and  $\varepsilon_{001}=(c_{\gamma}-a_P)/a_P$ , respectively.  $a_{\gamma}$  and  $c_{\gamma}$  are the lattice parameters of the  $\gamma$  phase, and  $a_P$  the lattice parameter of the P-type carbide phase. The data shows that the lattice mismatch along the c-axis of the  $\gamma$  phase,  $\varepsilon_{001}$ , is smaller than along either the a- or b-axis ( $\varepsilon_{100/010}$ ). P-type carbides are under compressive stress and this stress along the  $[001]$  direction is smaller than that along the other two cubic crystallographic orientations. Consequently P-type carbides in the  $\gamma$  matrix grow preferentially along the  $[001]$  direction. However, the difference in mismatch between  $\varepsilon_{001}$  and  $\varepsilon_{100/010}$  is less than that reported in the study of Tian et al. [11] and Schuster et al. [23]. This is probably due to different alloy compositions.

The morphology transformation to plates is very apparent in HIP+anneal specimens and has not been reported in previous work. It can be explained using predictions made by Lee et al. [24] based on the theory of Eshelby [25] for inclusions. They found that plates are the most energetically favorable shape for coherent precipitates during their growth if they are elastically softer and have a lower elastic anisotropy factor than the matrix. These pre-conditions are met in the present case. From literature data [26, 27] it can be estimated that the shear modulus of the P-type carbides is only around 0.8 that of

the  $\gamma$  matrix while the anisotropy factor of the  $\gamma$  matrix is roughly double that of P-type carbides.

Through quantifying the carbide size and number density during annealing some additional insight can be gained (**Fig. 3**). As particle splitting is observed after 168 h in the SOL+anneal condition the carbide number density and size are only plotted up to 96 h for this specimen condition. For both heat-treated conditions the carbide number density decreases and the carbide size increases with increasing annealing time. Nevertheless, it should be noted that the carbide number density in the SOL+anneal specimens is significantly higher and the size of the carbides is smaller. Solution treatment at 1250 °C results in dissolution of grain boundary carbides [19] and redistribution of carbon into the matrix. Thus, more carbides form in the  $\gamma$  matrix in the SOL+anneal specimens but grow slowly compared to carbides in the HIP+anneal specimens. Due to the fact that the plate thickness  $T$  at 48 h is smaller than the needle diameter  $D$  at 24 h in the HIP+anneal specimens the change from a needle- to a plate-like morphology cannot occur by anisotropic growth in a second direction. It is most probably associated with a redistribution of atoms.

### **3.2 Splitting of the perovskite $Ti_3AlC$ carbide**

As discussed above, perovskite  $Ti_3AlC$  carbides split after annealing at 800 °C for 168 h. After annealing for 1054 h, most carbides split completely into smaller sub-particles in the SOL+anneal condition. In the HIP+anneal condition, carbides also split similarly, although after 1054 h some carbides still retain in a plate-like shape. The different shape development of carbides in both conditions may be attributed to the combined effects from carbide density, chemical homogeneity and the stress field in which the carbides are situated. In the following the carbides in the SOL+anneal

specimens are further investigated to elucidate the splitting process and the split substructure configuration in detail.

### 3.2.1 Splitting process

Observation of the particle morphology in an intermediate state after 336 hours of annealing suggests that the conglomerates of carbide sub-particles stem from a splitting process. **Figure 4** shows the perovskite  $\text{Ti}_3\text{AlC}$  carbides in the SOL+anneal specimen after annealing for 336 h imaged along the  $[100]_\gamma$  (**Fig. 4a**) and  $[001]_\gamma$  (**Fig. 4b**) directions, respectively. The dark-field images were taken using a reflection from the precipitates and thus the carbides show bright contrast. As described earlier, after annealing for 1054 h the carbides split into smaller sub-particles. The conglomerates of sub-particles are arranged in a plate-like shape with the plate plane being either parallel to the  $(100)_\gamma$  (orientation type A in the following text) or  $(010)_\gamma$  (orientation type B) planes. When imaged along the  $[100]_\gamma$  direction using  $\mathbf{g}=010_P$  (**Fig. 4a**), type B sub-particle conglomerates are viewed from the side and type A sub-particle conglomerates are viewed from the top. The side-view of type B shows uniform contrast along the needle-like projections. For some top-views of type A, it is apparent that the carbides have only split into parallel needles elongated along the  $[001]_\gamma$  direction, as marked by arrows. However, it is also observed in other type A conglomerates that these parallel needles have started to further split into smaller sub-particles. When imaged along the  $[001]_\gamma$  direction using  $\mathbf{g}=010_P$  (P stands for perovskite  $\text{Ti}_3\text{AlC}$  phase, **Fig. 4b**), fringes not only appear in A type sub-particle conglomerates, but also in some of the B type.

In order to understand the nature of these fringes (i.e. the crystal volume between the split carbide sub-particles), tilting experiments and dark-field imaging utilizing different  $\mathbf{g}$ -vectors were conducted. By measuring the fringe spacing, it could be confirmed that

the contrast phenomena is not moiré fringes but indeed originates from the carbide splitting process. **Figure 5** shows examples imaged from the  $[001]_{\gamma}$  and the  $[100]_{\gamma}$  directions, respectively for a SOL+anneal specimen after annealing for 1054 h. From **Figs. 5a** and **b** ( $[001]_{\gamma}$ ), the projections of the two types of carbide sub-particle conglomerates are observable. When using  $g=100_P$ , all the regions between the sub-particles in type A show bright contrast as the sub-particles, while become dark at  $g=010_P$ . For carbide sub-particle conglomerates of type B the situation is reversed. When viewed along the  $[100]_{\gamma}$  direction (**Figs. 5c** and **d**), all the regions between sub-particles in type B show bright contrast using  $g=010_P$ , but lose the brightness when using  $g=01-1_P$ . Based on this diffraction analysis it is found that the regions between sub-particles also show bright contrast as the carbide sub-particles in some cases when using the precipitate diffractions in dark-field imaging. Thus it is proposed that the regions between carbide sub-particles have a different crystallographic orientation compared to the surrounding  $\gamma$  matrix. Also the orientation of the region between the sub-particles for each type of sub-particle conglomerate is different. Here it is also worth mentioning that the splitting phenomenon found in this work differs from that reported by Tian et al. [11], where long-range carbon-vacancy ordering was formed in the perovskite carbides. The phenomenon observed by Tian should not be visible as fringes under the imaging conditions used in this work.

From the results presented above we know that the splitting of carbides includes different stages: big carbides first split into parallel needles which are aligned along the  $[001]_{\gamma}$  lattice direction, then these parallel needles further split into small sub-particles, with the orientation of regions between carbide sub-particles changing. However, detailed information about the split substructure and the region between sub-particles is

still lacking. In order to clarify the atomic arrangement of the substructure and the interface between the sub-particles and the matrix, HRTEM investigations were carried out on specimens of SOL+anneal material.

### 3.2.2 Structure of the sub-particle conglomerates after splitting

The interface between the carbides and the  $\gamma$  matrix was investigated by HRTEM along different zone axes. The findings imply that the carbides remain coherent with the surrounding  $\gamma$  matrix during the course of ageing as no misfit dislocations are observed. It is interesting to note that a loss of coherency is reported already for 168 hours of annealing in the 800 °C temperature range in literature [10]. This discrepancy may stem from the fact that an alloy with higher aluminum and lower niobium content was investigated in [10] and the loss of coherency was coupled with a transformation to hexagonal (H-Ti<sub>2</sub>AlC) type carbides.

An investigation of the splitting process as well as the arrangement of the crystallographic phases within sub-particle conglomerates by high-resolution-imaging reveals, that the tetragonality and elastic anisotropy of the L1<sub>0</sub>  $\gamma$ -TiAl crystal structure fundamentally affects the process.

**Fig. 6a to c** show the cross-section of carbides at different stages of splitting after annealing for 168 h (imaged along the  $[001]_{\gamma}$ ). Most carbides are needle-shaped and show nearly octahedral cross-sections (**Fig. 6a**). Some other carbides have started to split in two parallel needles by an ingrowth of the  $\gamma$  matrix ( $\gamma_m$ ) phase which has resulted in a dumbbell-like cross-section. Only a small section of Ti<sub>3</sub>AlC carbide lattice structure remains and connects two parallel carbide needles, as seen in **Fig. 6b**. **Figure 6c** shows the carbide has fully split. In addition the crystallographic orientation of the region between the two parts has changed and is different to that of the surrounding

matrix. The region shows a contrast of alternating darker and brighter atomic planes. This is a view of the atomic structure of the  $L1_0$   $\gamma$ -TiAl phase along the [100] or [010] direction where the ordered structure of  $L1_0$  is visible. From the experimental observations by the dark-field imaging and HRTEM, the following order of events can be deduced: Carbides split into two or more parallel needles by the ingrowth of a small section of the  $\gamma_m$  matrix. Subsequently, this section of interspersed  $\gamma$  phase ( $\gamma_i$ ) between the needles crystallographically re-arranges from an initial [001] to a [100] or [010] orientation.

**Figure 7** shows two completely split-up carbide conglomerates as found after 1054 hours of annealing. **Figures 7a** and **b** are imaged along the [001] and [100] orientation of the surrounding  $\gamma$  matrix, respectively. In both micrographs regions of the  $\gamma_i$  phase with a crystallographic orientation different from the surrounding  $\gamma_m$  matrix are clearly discernible between the larger carbide sub-particles. The shape of the  $\gamma_i$  phase regions is not equiaxed. Interfaces with the carbide sub-particles are significantly larger than interfaces with the  $\gamma_m$  matrix resulting in a width-to-height ratio of about 3 to 1.

**Figure 8** shows the results of the atom probe investigation of a carbide sub-particle conglomerate in a SOL+anneal specimen after annealing for 1054 h. To delineate the particles, a 5 at.% iso-surface of carbon is shown together with an atom map of C in **Fig. 8a**. The TEM investigations above only show that the Ti and Al atoms in the carbide sub-particles are arranged in a way that is in alignment with the crystal structure of the P-Ti<sub>3</sub>AlC phase. The atom probe results furthermore reveal that this change in crystallography is also connected with an enrichment of carbon in the carbide sub-particles. The iso-concentration surface based on the APT data resembles the morphology of the carbide sub-particle conglomerates known from the TEM

micrographs. From the APT data, the chemical composition of the carbide phase and the matrix regions  $\gamma_m$  and  $\gamma_i$  (green box in **Fig. 8a**) were derived. A proximity histogram of concentration vs. distance to the iso-surface in **Fig. 8a** is shown in **Fig. 8b**. In order to exclude  $\gamma_i$  regions, the proximity histogram was calculated for the region marked in the inset only. The concentration for  $\gamma_i$  was calculated separately for the region in the green box and is included in the graph. The composition of  $\gamma_m$  with 46.7 at.% Ti, 47.6 at.% Al and 5.4 at.% Nb has nearly the same Nb content than results published in the literature for a similar alloy [28] but is leaner in Ti and higher in Al. Especially, the carbon content found in the matrix phase  $\gamma_m$  is significantly lower than in [28] and in better agreement with carbon contents reported in [29-31] for a number of single  $\gamma$ -phase and  $\alpha_2+\gamma$ -two phase alloys. It is interesting to note that the composition of  $\gamma_i$  differs from  $\gamma_m$ . While Ti is only slightly decreased to 43.9 at.% in  $\gamma_i$ , the carbon and oxygen concentration are increased to 2.9 and 4.1 at.%, respectively. While part of this enrichment may be caused by local magnification effects it is nevertheless higher than expected for  $\gamma$ -TiAl phase. Thus,  $\gamma_i$  from its crystallographic arrangement of Ti and Al atoms can be considered as a kind of  $\gamma$ -TiAl phase being not in thermodynamic equilibrium because the solubility of carbon as well as oxygen are exceeded. In the carbide sub-particles, the Ti-concentration is increased while the concentration of Al is decreased. The contents of Ti and Al agree well with literature data for the ternary Ti-Al-C system [32, 33]. According to them the stoichiometric Ti:Al ratio of 3:1 is nearly reached. Also the measured content of carbon in the carbide agrees with compositions reported in literature predicting P-type carbide contents for carbon lean ternary Ti-Al-C alloys to be slightly lower than the concentration of aluminum in the precipitate [32, 33]. Virtually no niobium is found in the carbide sub-particles.

### 3.2.3 Interpretation for carbide splitting

According to the classical coarsening theory larger precipitates grow at the expense of smaller ones during ageing to reduce the interfacial energy [34, 35]. However, if the precipitates remain coherent or semi-coherent with the matrix during the course of growth, the elastic strain energy cannot be ignored. In addition to the strain energy from the precipitate itself, there is elastic interaction energy due to the neighboring precipitates, which also affects the particle arrangement and shape [36, 37]. So, the energy state of a coherent carbide in the matrix is expressed as  $E = E_{elas} + E_{surf} + E_{int}$  [37-40]. Where,  $E_{elas}$  is the elastic strain energy due to the lattice mismatch between the carbide and the  $\gamma$  matrix,  $E_{surf}$  is the surface (interfacial) energy, and  $E_{int}$  is the elastic interaction energy caused by the overlap of elastic strain fields from individual coherent carbide precipitates. In the case that a large carbide precipitate splits into smaller carbide sub-particles and the shape of the individual particle or sub-particle is assumed as an ellipsoid of revolution, according to the theory of Eshelby [25] the energy state before (Eq. 1) and after splitting (Eq. 2) can be expressed by the following equations [37-40].

$$E_1 = V_1 * E_{elas} + S_1 * \gamma \quad \text{Eq. 1}$$

$$E_2 = N * \frac{V_1}{N} * E_{elas} + N * S_2 * \gamma + E_{int}^N \quad \text{Eq. 2}$$

where  $V_1$  is the volume and  $S_1$  is the surface area of a single carbide,  $E_{elas}$  is the elastic strain energy per unit volume and  $\gamma$  is the interfacial energy per unit area of the carbide precipitate,  $N$  is the number and  $S_2$  is the surface area of a single carbide sub-particle.  $E_{int}^N$  stands for the elastic interaction energy between the carbide sub-particles. If the aspect ratios of the single carbide and the carbide sub-particles do not differ very much, the elastic energy could be assumed to be the same before and after splitting analogous

to the situation reported in literature for the example of Ni-base superalloys [37-40]. Based on Eqs. 1-2, if a gain in elastic interaction energy can outbalance the increase of interfacial energy due to an increased interfacial area between the carbide and the  $\gamma$  phase, the total energy is reduced and splitting is energetically favourable.

A number of authors have predicted [37-42] by theoretical calculation that splitting of a large precipitate into smaller sub-particles can be energetically favourable in Ni-base superalloys due to elastic interaction between the sub-particles. In this paper, we did not carry out such theoretical calculations for the elastic interaction energy but qualitatively applied the results from Ni-base superalloys for our case. Due to the tetragonal crystal structure of the  $\gamma$ -TiAl matrix the necessary calculations are more complicated as in the case of the cubic Ni-matrix and would be beyond the scope of this experimental paper. So, we refrain ourselves to a qualitative comparison with the results from Ni-base superalloys. The authors in [37-42] consider a large particle that splits into an agglomerate of smaller particles. They calculate the elastic interaction energy as well as the energy needed to create new matrix/sub-particle interfaces for the formation of an agglomerate of sub-particles from an initially large particle. Their results show that, if the newly formed sub-particles are arranged along elastically soft directions of the matrix phase, and if at the same time the anisotropy factor  $A = 2C_{44}/(C_{11} - C_{12})$  of the matrix is larger than one, then an arrangement of smaller spherical or plate shaped (sub-) particles can lead to an energy reduction. Both conditions are met for our case with the  $\langle 001 \rangle$  directions of the  $\gamma$ -TiAl phase being the elastically softest compared to for example  $\langle 110 \rangle$  or  $\langle 111 \rangle$  and  $A = 1.92$  (He et al. [27]). Thus, in accordance with the aforementioned calculations [39-42] a reduction in overall energy due to the elastic interaction between sub-particles can account for the splitting of large P-type carbides.

However, probably due to the tetragonal crystal structure of the  $\gamma$ -TiAl matrix, P-type carbides first split along the [001] direction to form parallel needles, and then these needles split further along the [100] or the [010] direction into smaller carbide sub-particles.

A number of investigations have shown the splitting of  $\gamma'$  precipitates in nickel-based superalloys when the  $\gamma'$  precipitates were sparsely distributed in the matrix [37-39, 43]. However, some workers believed this finding resulted from a coalescence of particles belonging to the same domain [44, 45]. These two processes are difficult to distinguish in those studies because precipitates, which were identified as split particles, were only slightly smaller in diameter (by a factor of about two) compared to the average diameter of precipitates for the respective annealing temperature and time. In the present study the evidence for a splitting of the P-type carbides is much stronger, because the sub-particles are significantly smaller (by a factor of about five to ten) than the carbide precipitates from which they form. Shape instability has also been reported in some composite systems for cylindrical structures or plate-shaped dispersions [46] and in TiAl based alloys with a lamellar structure [47]. A cylindrical fiber embedded in a matrix with longitude perturbation in radius is not stable and will be spheroidized when the magnitude between the neighboring perturbations (wavelength of perturbation,  $\lambda$ ) exceeds a critical wavelength  $\lambda_{crit}=2\pi r_0$  ( $r_0$  is the radius of the unperturbed cylinder) [46]. This perturbation method was developed by Lord Rayleigh to examine the phenomenon of a liquid cylinder breaking into small droplets [48]. For plate-shaped dispersions, there are three clearly identified primary modes of instability: cylinderization, boundary splitting and edge spheroidization. The dominant instability mechanism for the plate morphology depends on several factors such as plate aspect

ratio (width/thickness) and dihedral angle ( $2\theta = 2 \cos^{-1} \gamma_B / 2\gamma_S$ ,  $\gamma_B$  is the internal boundary surface energy and  $\gamma_S$  is the interphase surface energy) at the triple point of the internal-external boundary juncture [46, 49]. In the case presented here lattice defects were rarely detected in carbide precipitates during the HRTEM investigations. Thus, the existence of internal faults which could act as preferred splitting sites as a necessary pre-requisite for splitting can be excluded. One could thus speculate that Rayleigh instabilities play a role when the carbide needles further split into smaller sub-particles during the second stage of splitting.

The crystallographic re-arrangement of the  $\gamma_i$  phase between the carbide sub-particles is most probably associated with the second part of the splitting process, i.e. the separation of the parallel needles into smaller sub-particles along their long axis. Only in conjunction with this step can such a crystallographic re-arrangement be helpful in reducing the coherency stresses between the  $\gamma_i$  phase and the carbide sub-particles. The initial crystallographic alignment of the c-axis of the  $\gamma_m$  phase is parallel to the long axis of the carbide needles and remains the energetically most favourable configuration for two or more parallel needles. However, when such parallel needles subsequently split into sub-particles along their long axis, this orientation of the  $\gamma_m$  c-axis is unfavourable for regions between the sub-particles. By assuming a new crystallographic orientation the  $\gamma_i$  phase between the sub-particles can reduce its mismatch with the P-type carbide lattice. This however is achieved at the cost of a new interface between the  $\gamma_i$  and the  $\gamma_m$  matrix regions which are now differently oriented to each other. Despite of the associated additional interfacial energies and coherency stresses the resulting arrangement can still be overall energetically favourable. Firstly, the lattice mismatch between the two crystallographically different types of  $\langle 001 \rangle$  directions in the  $L1_0$   $\gamma$ -

TiAl phase is lower than that between the  $\gamma$ -TiAl phase and the P-type carbide phase. Additionally, the carbide sub-particles and the  $\gamma_i$  volume segments assume a morphology which results in larger interfacial areas between the  $\gamma_i$  and the P-type carbide than those between the  $\gamma_i$  and the  $\gamma_m$  matrix. So the  $\gamma_i$  regions reorient in a way where the areas with relatively low mismatch between  $\gamma_i$ ,  $\gamma_m$  and P-type carbide are maximised. However, it cannot be determined from the experimental results if the rearrangement of the  $\gamma_i$  phase takes place simultaneously with the second step of splitting, or occurs subsequently to the parallel needles splitting into smaller sub-particles along their long axes.

In this study, the morphology of the P-type carbides in TiAl alloys changes during exposure to typical service temperatures. Due to different thermal history, the local carbon concentration varies and influences the evolution of the carbide morphology. This morphology change should be considered for the practical application of carbide precipitate-strengthening of TiAl alloys. However, how the morphology change, especially the split up of coarse carbides into smaller carbide sub-particles influences the mechanical properties must remain to be answered by further studies. One could speculate that the interaction between dislocations and a carbide sub-particle conglomerate may not be different to the one of a dislocation and a solid carbide. Thus, neither a positive nor a negative effect would be expected. Nevertheless, the combination of carbide sub-particles with interspersed matrix regions oriented differently from the surrounding  $\gamma$  matrix could be beneficial in two ways. Firstly, the hardening species now consists of the carbide phase and part of the  $\gamma$  phase exhibiting a higher overall volume fraction of hardening phase compared to the carbide phase acting alone. Secondly, as the formation of carbide conglomerates seems to be energetically

beneficial the existence of such a morphology could hinder or delay further carbide coarsening being detrimental for hardening. Both assumptions are of course only valid when comparing the carbide conglomerates with equally coarse or coarser solid carbides. There is no reason to assume that the hardening effect of the carbide conglomerates should be higher than a homogeneous distribution of the sub-particles as small separated carbide precipitates in the matrix.

#### **4. Conclusions**

Coherently embedded perovskite precipitates in  $\gamma$ -TiAl undergo a morphology change from needles to conglomerates of smaller sub-particles which form due to the splitting of precipitates. To our knowledge this is the first work in which such splitting of precipitates has been observed in a matrix phase with a tetragonal crystal structure. The morphology change increases the surface area between the precipitate phase and the matrix and is thus counter intuitive on first sight. Nevertheless, theoretical literature studies of similar precipitate configurations suggest that such an arrangement can be energetically favourable due to the elastic interaction between the carbide sub-particles. Understanding  $Ti_3AlC$  carbide morphology development and splitting is of importance to improve the mechanical properties of TiAl alloys. The main conclusions are following.

1. The morphology of coherently embedded P-type carbides undergoes a series of transformations involving growth and coarsening in order to minimize the elastic distortion energy.
2. The exact carbide morphology development differs in the two heat-treated conditions. Carbides change shape from needles to plates prior to splitting in the HIP+anneal

condition, while in the SOL+anneal condition no clearly developed plate shape was observed prior to splitting. This shows the strong sensitivity of the carbide morphology development to changes in local carbon concentration caused by different heat treatment history.

3. During ageing larger carbides decompose into smaller sub-particles; this is an energetically favored configuration that results from the elastic interaction energy between the split sub-particles. The splitting takes place in two separate steps: firstly big carbides split into several parallel needles, and then these needles split further into smaller sub-particles. Due to the morphology of the original precipitates it has been unambiguously shown that the conglomerate of sub-particles indeed arises due to a splitting phenomenon and does not originate from a coalescence of small precipitates.

4. Due to the tetragonality of the  $L1_0$   $\gamma$ -TiAl matrix phase, the region of the  $\gamma_i$  phase between the split sub-particles reorients to minimize the lattice mismatch at its interface with the carbide sub-particles.

### **Acknowledgement**

The authors are grateful to Dr. Michael Oehring and Dr. Jonathan Paul for their help, and Dr. Frank-Peter Schimansky and Dirk Matthiessen for producing the HIPed pre-alloyed powder. Li Wang acknowledges the Chinese Scholarship Council and the Helmholtz Association for funding her PhD project at Helmholtz-Zentrum Geesthacht in framework of the CSC-Helmholtz program.

### **Reference**

- [1] B.P. Bewlay, M. Weimer, T. Kelly, A. Suzuki, P.R. Subramanian, The Science, Technology, and Implementation of TiAl Alloys in Commercial Aircraft Engines, MRS Online Proceedings Library, 1516 (2013) 49-58.
- [2] H. Clemens, W. Wallgram, S. Kremmer, V. Güther, A. Otto, A. Bartels, Design of Novel  $\beta$ -Solidifying TiAl Alloys with Adjustable  $\beta$ /B2-Phase Fraction and Excellent Hot-Workability, *Adv. Eng. Mater.*, 10 (2008) 707-713.
- [3] W.J. Zhang, S.C. Deevi, G.L. Chen, On the origin of superior high strength of Ti-45Al-10Nb alloys, *Intermetallics*, 10 (2002) 403-406.
- [4] F. Appel, M. Oehring, R. Wagner, Novel design concepts for gamma-base titanium aluminide alloys, *Intermetallics*, 8 (2000) 1283-1312.
- [5] J.P. Lin, L.L. Zhao, G.Y. Li, L.Q. Zhang, X.P. Song, F. Ye, G.L. Chen, Effect of Nb on oxidation behavior of high Nb containing TiAl alloys, *Intermetallics*, 19 (2011) 131-136.
- [6] M. Nemoto, W.H. Tian, K. Harada, C.S. Han, T. Sano, Microstructure of precipitation strengthened Ni<sub>3</sub>Al and TiAl, *Mater. Sci. Eng., A*, 152 (1992) 247-252.
- [7] U. Christoph, F. Appel, R. Wagner, Dislocation dynamics in carbon-doped titanium aluminide alloys, *Mater. Sci. Eng., A*, 239–240 (1997) 39-45.
- [8] F. Appel, Fischer, F. D., Clemens, H., Precipitation twinning, *Acta Mater.*, 55 (2007) 4915-4923.
- [9] F. Appel, J.D.H. Paul, M. Oehring, *Gamma Titanium Aluminide Alloys: Science and Technology*, Wiley-VCH, Weinheim, Germany 2011.
- [10] S. Chen, P.A. Beaven, R. Wagner, Carbide precipitation in  $\gamma$ -TiAl alloys, *Scr. Metall. Mater.*, 26 (1992) 1205-1210.

- [11] W.H. Tian, T. Sano, M. Nemoto, Structure of perovskite carbide and nitride precipitates in L1<sub>0</sub>-ordered TiAl, *Philos. Mag. A*, 68 (1993) 965-976.
- [12] S.A. Gerstl, D. Seidman, Chemical and Structural Investigation of Internal Domains of Needle-Like Ti<sub>3</sub>AlC Carbide Precipitates in gamma-TiAl with 3-D Atom Probe Tomography, *Microsc. Microanal.*, 12 (2006) 1570-1571.
- [13] Y. Wu, Y.W. Park, H.S. Park, S.K. Hwang, Microstructural development of indirect-extruded TiAl-Mn-Mo-C intermetallic alloys during aging, *Mater. Sci. Eng., A*, 347 (2003) 171-179.
- [14] R.J. Simpkins, M.P. Rourke, T.R. Bieler, P.A. McQuay, The effects of HIP pore closure and age hardening on primary creep and tensile property variations in a TiAl XD(TM) alloy with 0.1 wt.% carbon, *Mater. Sci. Eng., A*, 463 (2007) 208-215.
- [15] P.A. McQuay, R. Simpkins, D.Y. Seo, T.R. Bishop, Alloy and process improvements for cast TiAl alloy applications, in: Y.-W. Kim, D.M. Dimiduk, M.H. Loretto (Eds.) *Gamma Titanium Aluminides TMS*, San Diego, California, 1999, pp. 197-207.
- [16] H.S. Park, S.K. Hwang, C.M. Lee, Y.C. Yoo, S.W. Nam, N.J. Kim, Microstructural refinement and mechanical properties improvement of elemental powder metallurgy processed Ti-46.6Al-1.4Mn-2Mo alloy by carbon addition, *Metall. Mater. Trans. A*, 32 (2001) 251-259.
- [17] R. Gerling, H. Clemens, F.P. Schimansky, Powder Metallurgical Processing of Intermetallic Gamma Titanium Aluminides, *Adv. Eng. Mater.*, 6 (2004) 23-38.
- [18] H. Gabrisch, A. Stark, F.P. Schimansky, L. Wang, N. Schell, U. Lorenz, F. Pyczak, Investigation of carbides in Ti-45Al-5Nb-xC alloys ( $0 \leq x \leq 1$ ) by transmission electron microscopy and high energy-XRD, *Intermetallics*, 33 (2013) 44-53.

- [19] L. Wang, H. Gabrisch, U. Lorenz, F.-P. Schimansky, A. Schreyer, A. Stark, F. Pyczak, Nucleation and thermal stability of carbide precipitates in high Nb containing TiAl alloys, *Intermetallics*, 66 (2015) 111-119.
- [20] L. Wang, Mechanisms of carbide precipitation and carbon solubility in high Nb containing TiAl Alloys, in, BTU Cottbus – Senftenberg <http://opus4.kobv.de/opus4-btu/frontdoor/index/index/docId/3039>, 2014.
- [21] K. Thompson, D. Lawrence, D.J. Larson, J.D. Olson, T.F. Kelly, B. Gorman, In situ site-specific specimen preparation for atom probe tomography, *Ultramicroscopy*, 107 (2007) 131-139.
- [22] P.J. Felfer, T. Alam, S.P. Ringer, J.M. Cairney, A reproducible method for damage-free site-specific preparation of atom probe tips from interfaces, *Microsc. Res. Techniq.*, 75 (2012) 484-491.
- [23] J.C. Schuster, H. Nowotny, C. Vaccaro, The ternary systems: CrAlC, VAlC, and TiAlC and the behavior of H-phases ( $M_2AlC$ ), *J. Solid State Chem.*, 32 (1980) 213-219.
- [24] J.K. Lee, D.M. Barnett, H.I. Aaronson, The elastic strain energy of coherent ellipsoidal precipitates in anisotropic crystalline solids, *Metall. Trans. A*, 8 (1977) 963-970.
- [25] J.D. Eshelby, The Determination of the Elastic Field of an Ellipsoidal Inclusion, and Related Problems, *Proceedings of the Royal Society of London. Series A. Mathematical and Physical Sciences*, 241 (1957) 376-396.
- [26] X. Zhang, X.H. Wang, F.Z. Li, Y.C. Zhou, Mechanical and thermal properties of antierovskite  $Ti_3AlC$  prepared by a in situ reaction/hot-pressing route, *J. Am. Ceram. Soc.*, 92 (2009) 2698-2703.

- [27] Y. He, R.B. Schwarz, T. Darling, M. Hundley, S.H. Whang, Z.M. Wang, Elastic constants and thermal expansion of single crystal  $\gamma$ -TiAl from 300 to 750 K, *Mater. Sci. Eng., A*, 239–240 (1997) 157-163.
- [28] C. Scheu, E. Stergar, M. Schober, L. Cha, H. Clemens, A. Bartels, F.P. Schimansky, A. Cerezo, High carbon solubility in a  $\gamma$ -TiAl-based Ti–45Al–5Nb–0.5C alloy and its effect on hardening, *Acta Mater.*, 57 (2009) 1504-1511.
- [29] A. Menand, A. Huguet, A. Nérac-Partaix, Interstitial solubility in  $\gamma$  and  $\alpha_2$  phases of TiAl-based alloys, *Acta Mater.*, 44 (1996) 4729-4737.
- [30] S. Kim, G.D.W. Smith, S.G. Roberts, A. Cerezo, Alloying elements characterisation in  $\gamma$ -based titanium aluminides by APFIM, *Mater. Sci. Eng., A*, 250 (1998) 77-82.
- [31] G.W. Qin, G.D.W. Smith, B.J. Inkson, R. Dunin-Borkowski, Distribution behaviour of alloying elements in  $\alpha_2(\alpha)/\gamma$  lamellae of TiAl-based alloy, *Intermetallics*, 8 (2000) 945-951.
- [32] M.A. Pietzka, J.C. Schuster, Summary of constitutional data on the Aluminum-Carbon-Titanium system, *J. Phase Equilib.*, 15 (1994) 392-400.
- [33] V.T. Witusiewicz, B. Hallstedt, A.A. Bondar, U. Hecht, S.V. Slepsov, T.Y. Velikanova, Thermodynamic description of the Al–C–Ti system, *J. Alloy. Compd.*, 623 (2015) 480-496.
- [34] H. Grätz, Classical theory of steady-state coarsening: A novel mathematical treatment of the basic equations, *Scripta Mater.*, 34 (1996) 1209-1217.
- [35] W. Ostwald, On the supposed isomerism of red and yellow mercury oxide and the surface tension of solid substances, *Z. Phys. Chem.*, 34 (1900) 495-503.

- [36] W.C. Johnson, P.W. Voorhees, Elastic interaction and stability of misfitting cuboidal inhomogeneities, *J. Appl. Phys.*, 61 (1987) 1610-1619.
- [37] T. Miyazaki, H. Imamura, T. Kozakai, The formation of " $\gamma'$  precipitate doublets" in Ni-Al alloys and their energetic stability, *Mater. Sci. Eng.*, 54 (1982) 9-15.
- [38] M. Doi, T. Miyazaki, T. Wakatsuki, The effect of elastic interaction energy on the morphology of  $\gamma'$  precipitate in Ni-based alloys, *Mater. Sci. Eng.*, 67 (1984) 247-253.
- [39] M. Doi, T. Miyazaki, T. Wakatsuki, The effects of elastic interaction energy on the  $\gamma'$  precipitate morphology of continuously cooled Nickel-base alloys, *Mater. Sci. Eng.*, 74 (1985) 139-145.
- [40] M. Doi, Coarsening Behaviour of Coherent Precipitates in Elastically Constrained Systems -With Particular Emphasis on Gamma-Prime Precipitates in Nickel-Base Alloys&mdash, *Mater. Trans., JIM*, 33 (1992) 637-649.
- [41] W. Johnson, Lee, JongK, Elastic interaction energy of two spherical precipitates in an anisotropic matrix, *Metall. Trans. A*, 10 (1979) 1141-1149.
- [42] T. Miyazaki, H. Imamura, H. Mori, T. Kozakal, Theoretical and experimental investigations on elastic interactions between  $\gamma'$ -precipitates in a Ni-Al alloy, *J. Mater. Sci*, 16 (1981) 1197-1203.
- [43] M. Doi, Elasticity effects on the microstructure of alloys containing coherent precipitates, *Prog. Mater. Sci.*, 40 (1996) 79-180.
- [44] D. Banerjee, R. Banerjee, Y. Wang, Formation of split patterns of  $\gamma'$  precipitates in Ni-Al via particle aggregation, *Scripta Mater.*, 41 (1999) 1023-1030.
- [45] H.A. Calderon, J.G. Cabanas-Moreno, T. Mori, Direct evidence that an apparent splitting pattern of gamma particles in Ni alloys is a stage of coalescence, *Philos. Mag. Lett.*, 80 (2000) 669-674.

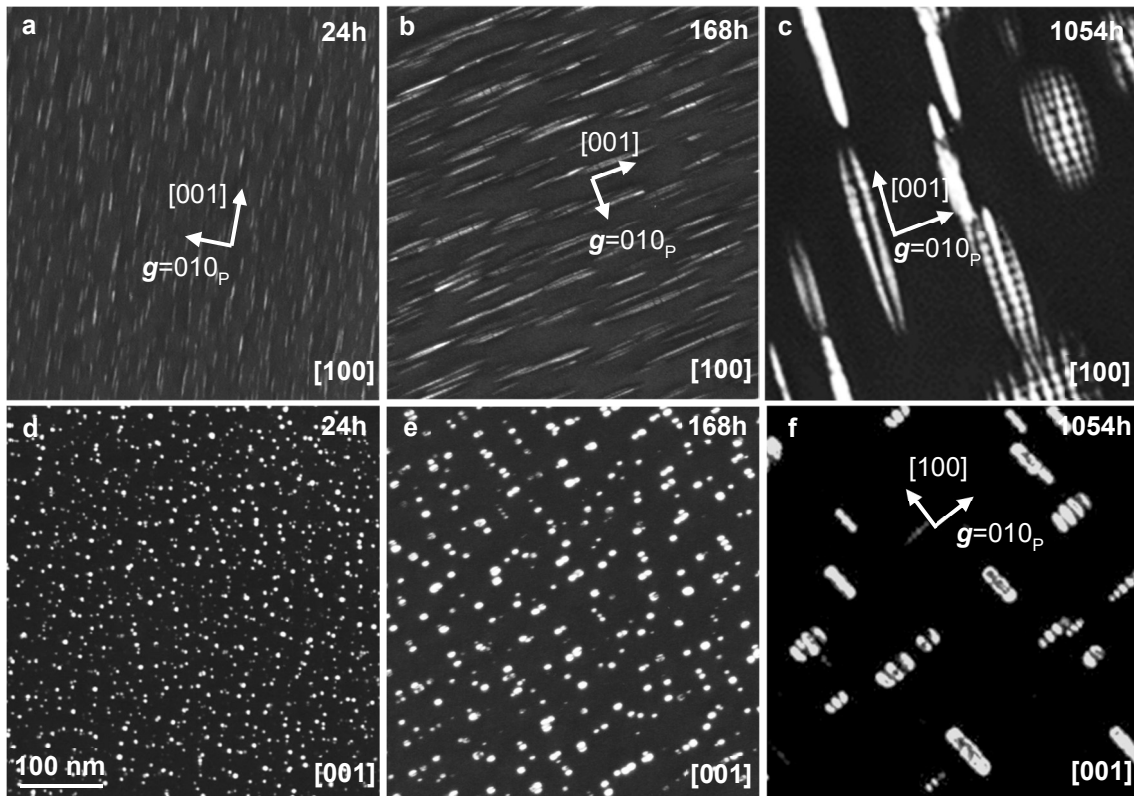
- [46] J.C.M. Kampe, T.H. Courtney, Y. Leng, Shape instabilities of plate-like structures—I. Experimental observations in heavily cold worked in situ composites, *Acta Metall.*, 37 (1989) 1735-1745.
- [47] G. Sharma, R.V. Ramanujan, G.P. Tiwari, Instability mechanisms in lamellar microstructures, *Acta Mater.*, 48 (2000) 875-889.
- [48] L. Rayleigh, On The Instability Of Jets, *Proceedings of the London Mathematical Society*, s1-10 (1878) 4-13.
- [49] T.H. Courtney, J.C.M. Kampe, Shape instabilities of plate-like structures—II. Analysis, *Acta Metall.*, 37 (1989) 1747-1758.

**Table 1** Lattice mismatch between the P-Ti<sub>3</sub>AlC and  $\gamma$  phases in the Ti-45Al-5Nb-0.75C alloy

	Heat-treated conditions	$a$		$c$		$\varepsilon_{100}$ (%)	$\varepsilon_{001}$ (%)
		P / $\gamma$ (Å)					
HIP+anneal	800 °C, 24 h	4.16 / 4.02	4.16 / 4.07	-3.37	-2.16		
	800 °C, 168 h	4.15 / 4.01	4.15 / 4.06	-3.37	-2.17		
SOL+anneal	1250 °C, 5 h + 800 °C, 24 h	4.15 / 4.02	4.15 / 4.07	-3.13	-1.93		
	1250 °C, 5 h + 800 °C, 168 h	4.15 / 4.02	4.15 / 4.07	-3.13	-1.93		

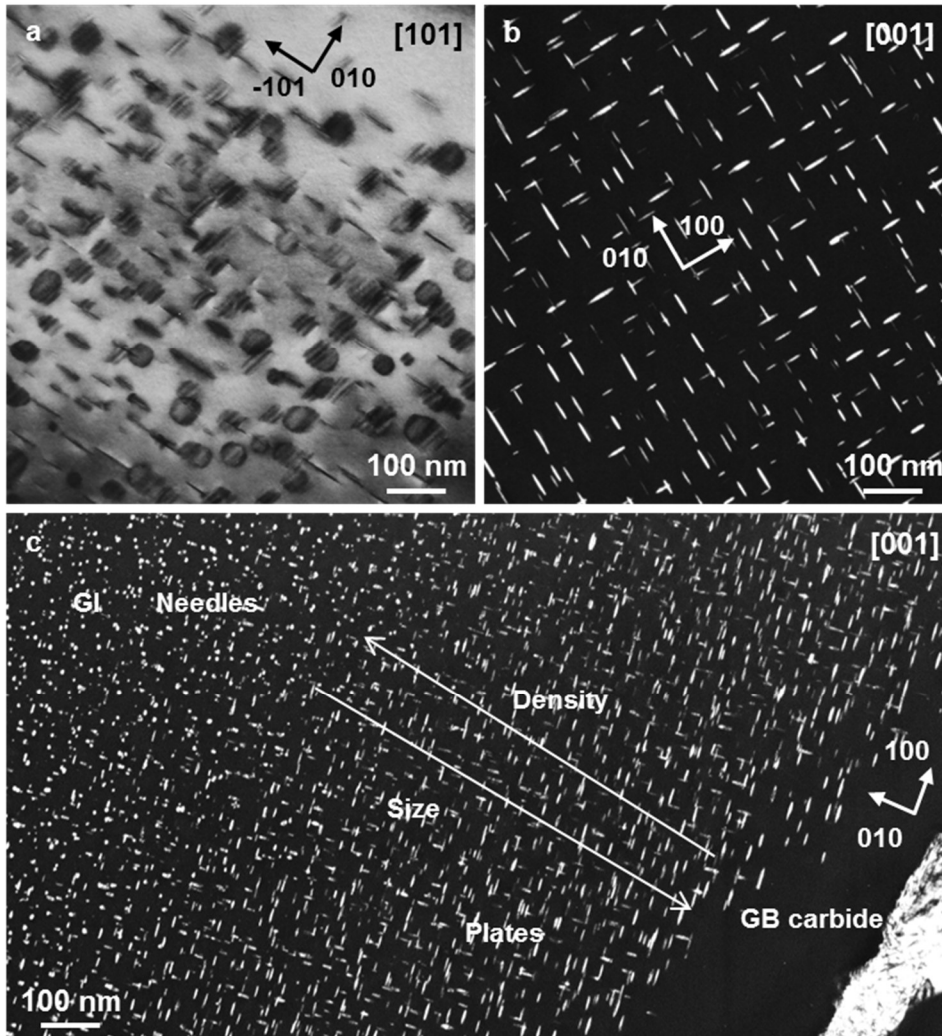
$a$  and  $c$  are lattice parameters of the unit cell for both the P-type carbide and the  $\gamma$  phase.

$\varepsilon_{100}$  and  $\varepsilon_{001}$  are lattice mismatch between the P-type carbide and the  $\gamma$  phase along the  $[100]_{\gamma}$  and  $[001]_{\gamma}$  crystallographic orientations.

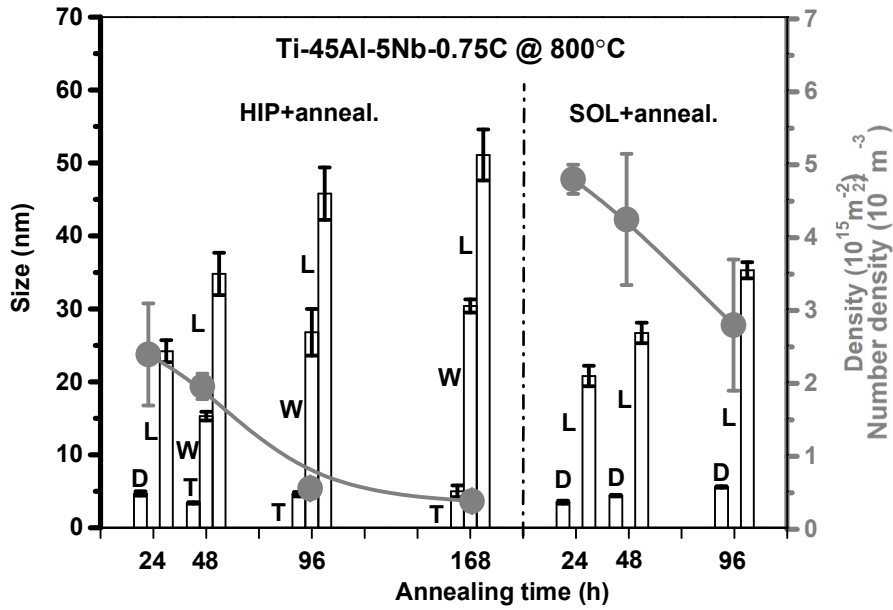


**Fig. 1.** Morphological development of  $\text{Ti}_3\text{AlC}$  carbides in the  $\gamma$  matrix of SOL+anneal specimens after solution treatment at  $1250\text{ }^\circ\text{C}$  for 5 h and subsequent annealing at  $800\text{ }^\circ\text{C}$  for (a, d) 24 h, (b, e) 168 h, (c, f) 1054 h.

The images in a-c were taken near the  $[100]_\gamma$  direction, while those in d-f were taken near the  $[001]_\gamma$  direction. TEM dark field images were recorded using  $010_p$  diffraction in the two-beam condition. All images have the same magnification.

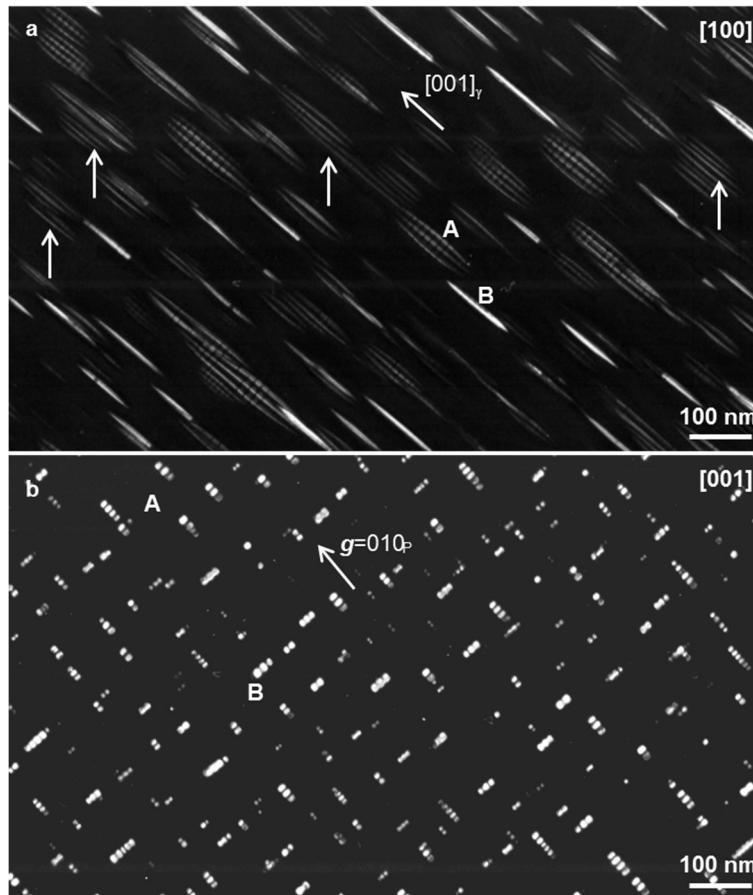


**Fig. 2.**  $\text{Ti}_3\text{AlC}$  carbides in the  $\gamma$  matrix of HIP+anneal specimens. (a) in the  $[101]_\gamma$  direction and (b) near the  $[001]_\gamma$  direction after annealing at  $800\text{ }^\circ\text{C}$  for 168 h. (c) near the  $[001]_\gamma$  direction after annealing at  $800\text{ }^\circ\text{C}$  for 48 h. GB: grain boundary; GI: grain interior. All TEM dark field images were recorded using  $010_{\text{P}}$  diffraction in the two-beam condition.

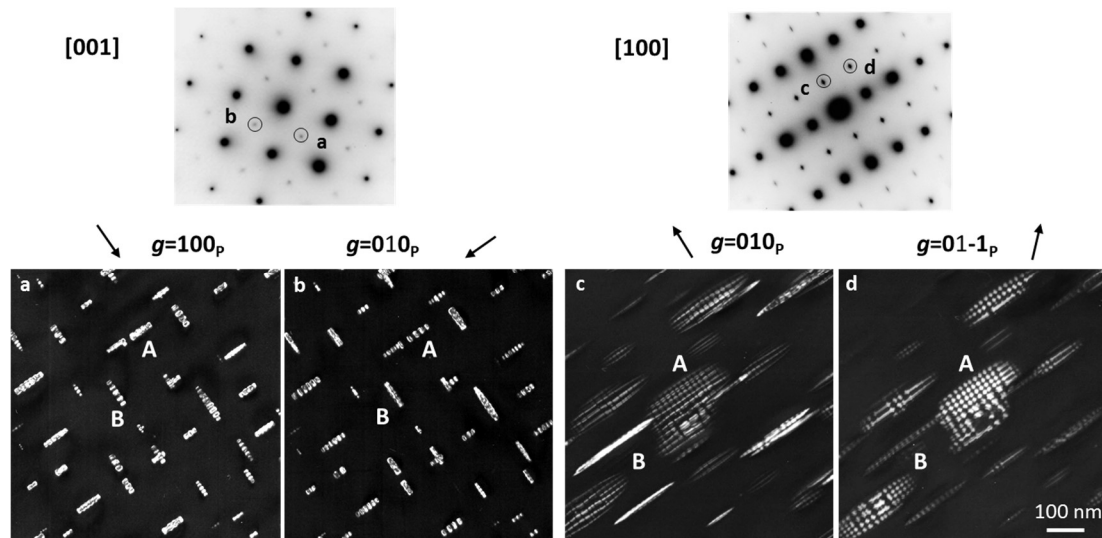


**Fig. 3.** Development of the carbide size and number density (with standard deviation bars) in the  $\gamma$  matrix as a function of annealing time at 800 °C in the Ti-45Al-5Nb-0.75C alloy.

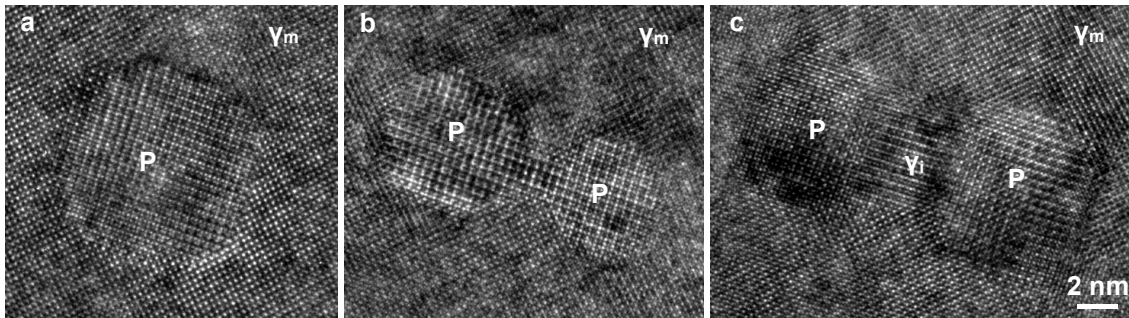
L, W and T represent Length, Width and Thickness for plates. L and D represent Length and Diameter for needles. Carbide number density is displayed as round symbols connected by a spline to guide the eye.



**Fig. 4.** Ti<sub>3</sub>AlC carbides in the  $\gamma$  matrix of a SOL+anneal specimen after solution treatment at 1250 °C for 5 h and subsequent annealing at 800 °C for 336 h. Dark-field images were recorded using  $g=010_p$  in the two-beam condition near (a) the  $[100]_\gamma$  direction and (b) the  $[001]_\gamma$  direction. A and B mark carbide sub-particle conglomerates which extend in the  $(100)_\gamma$  and  $(010)_\gamma$  planes, respectively. Arrows mark carbides which have only split into parallel needles.

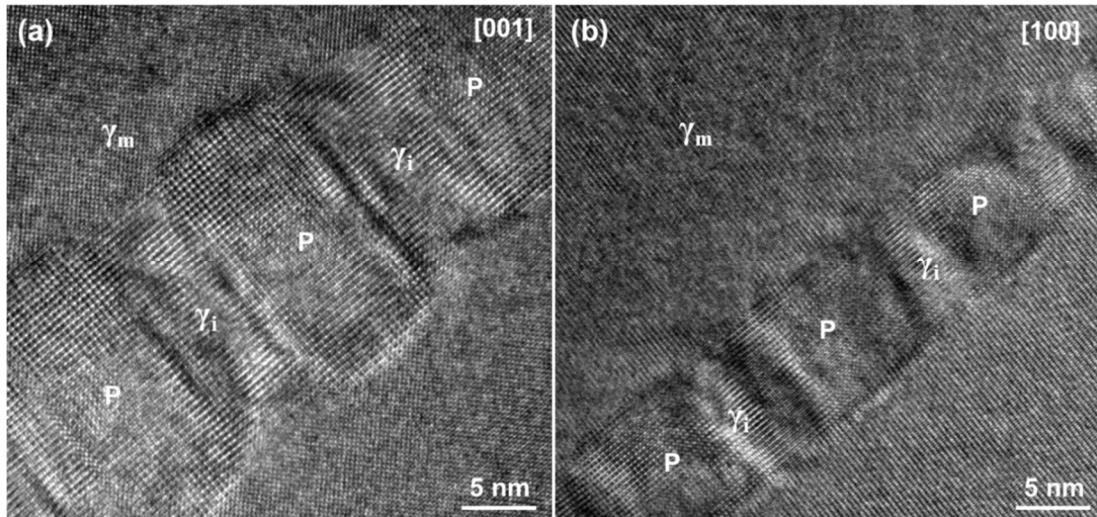


**Fig. 5.** Dark-field imaging of  $\text{Ti}_3\text{AlC}$  carbides in the  $\gamma$  matrix of a SOL+anneal specimen after solution treatment at  $1250\text{ }^\circ\text{C}$  for 5 h and subsequent annealing at  $800\text{ }^\circ\text{C}$  for 1054 h. The images were taken along the  $[001]_\gamma$  direction using (a)  $g=100_p$  and (b)  $g=010_p$ , and along the  $[100]_\gamma$  direction using (c)  $g=010_p$  and (d)  $g=01-1_p$ . A and B mark carbide sub-particle conglomerates which extend in the  $(100)_\gamma$  and  $(010)_\gamma$  planes, respectively. All dark-field images have the same magnification.



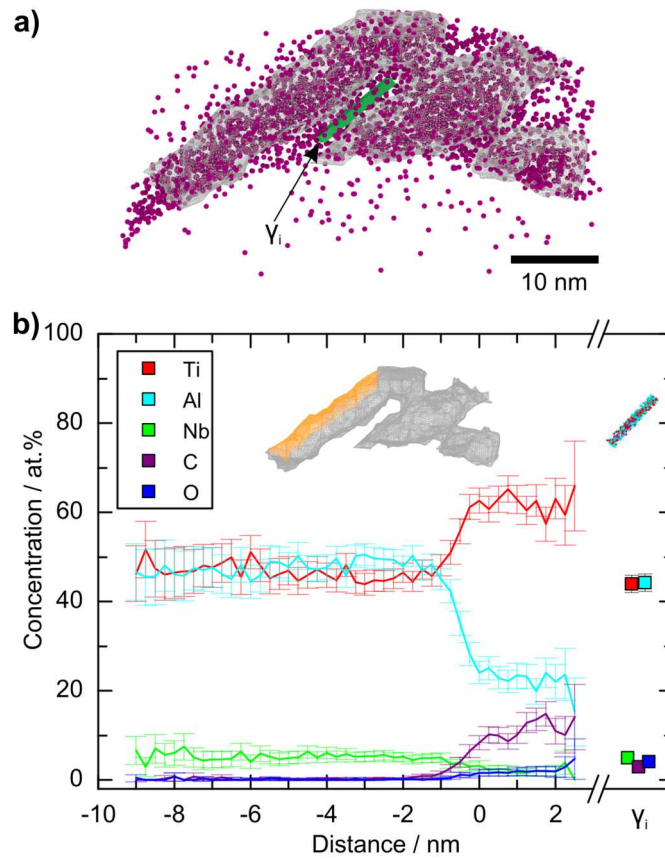
**Fig. 6.** Different stages of the carbide splitting process in a SOL+anneal specimen after solution treatment at 1250 °C for 5 h and subsequent annealing at 800 °C for 168 h, viewed along the  $[001]_{\gamma}$  direction.

(a) A needle-shaped carbide shows nearly octahedral cross-section, (b) a carbide has started to split due to the ingrowth of the surrounding  $\gamma$  matrix, (c) a carbide has fully split and the region of the  $\gamma$  phase between sub-particles has reoriented with respect to the surrounding  $\gamma$  matrix.



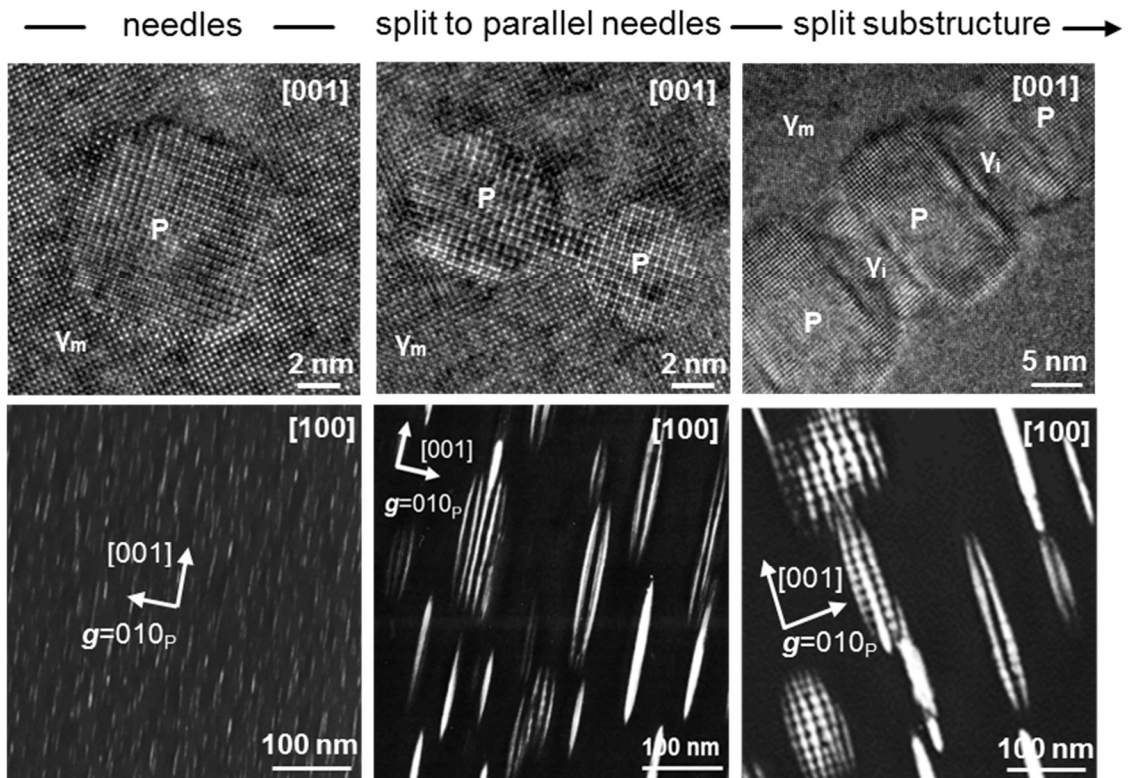
**Fig. 7.** Details of carbide sub-particle conglomerates in a SOL+anneal specimen after solution treatment at 1250 °C for 5 h and subsequent annealing at 800 °C for 1054 h.

(a) Imaged along the  $[001]_{\gamma}$  orientation; (b) Imaged along the  $[100]_{\gamma}$  orientation.



**Fig. 8.** Atom probe investigation of a carbide sub-particle conglomerate in a SOL+anneal specimen after solution treatment at 1250 °C for 5 h and subsequent annealing at 800 °C for 1054 h. (a) atom map of carbon with a 5 at.% carbon iso-surface. (b) proximity histogram of elemental concentration vs. distance to the iso-surface in (a), compared to the concentrations in the  $\gamma_i$  region (green box in Fig. 8a) .

Graphical abstract



Morphology development of P-Ti<sub>3</sub>AlC carbides with time